Journal of Biomechanics 107 (2020) 109844

Contents lists available at ScienceDirect

Journal of Biomechanics

journal homepage: www.elsevier.com/locate/jbiomech
www.JBiomech.com

Explicit finite element analysis can predict the mechanical response of conical implant press-fit in homogenized trabecular bone

Marzieh Ovesy *, Marcel Aeschlimann, Philippe K. Zysset

ARTORG Centre for Biomedical Engineering Research, University of Bern, Freiburgstrasse 3, 3010 Bern, Switzerland

ARTICLE INFO

Article history:
Accepted 8 May 2020

Keywords:
Explicit finite element analysis
Homogenized bone properties
Press-fit
Damage
Implant insertion
Primary stability

ABSTRACT

Prediction of primary stability is a major challenge in the surgical planning of dental and orthopedic implants. Computational methods become attractive to estimate primary stability from clinical CT images, but implicit finite element analysis of implant press-fit faces convergence issues due to contact and highly distorted elements. This study aims to develop and validate an explicit finite element method to simulate the insertion and primary stability of a rigid implant in a deformable bone while accounting for damage occurring at the bone-implant interface. Accordingly, a press-fit experiment of a conical implant into predrilled bovine trabecular bone was designed and realized for six samples. A displacement-driven cyclic protocol was used to quantify the reaction force and stiffness of the bone-implant system. Homogenized finite element analyses of the experiments were performed by modeling contact with friction and converting an existing constitutive model with elasto-plasticity and damage of bone tissue to be applicable to an explicit time integration scheme where highly distorted elements get deleted. The computed reaction forces and unloading stiffnesses showed high correlations (R^2 = 0.95 and R^2 = 0.94) with the experiment. Friction between bone and implant exhibited a strong influence on both reaction force and stiffness. In conclusion, the developed explicit finite element approach with frictional contact and element deletion accounts properly for bone damage during press-fit and will help optimizing dental or orthopedic implant design towards maximal primary stability.

1. Introduction

The long term success of uncemented total hip arthroplasty is dependent on both the short term healing time following the surgery during in the implant must sustain loads without bone damage (primary stability) and the long term osseointegration of the bone into the implant that must prevent loosening (secondary stability) (Mjöberg, 1997; Wyatt et al., 2014). Primary stability can be assessed by stiffness and the micromotions occurring at the bone-implant interface, where both later affect the extent of secondary stability (Pilliar et al., 1986; Jasty et al., 1997). The time and cost of the experiments, the variability associated with human tissue and the difficulty of modeling complex loading protocols foster the use of *in silico* modeling for stability assessment (Reggiani et al., 2007; van der Ploeg et al., 2012; Bah et al., 2015). Finite element analyses (FEA) of bone-implant systems are conducted by using implicit or explicit solver schemes. Implicit FEA models bone either by accounting for the microarchitecture (micro-FE) (van Rietbergen and Ito, 2015) or by assigning homogenized material properties through a continuous mesh (Charlebois et al., 2010; Hosseini et al., 2012; Schwiedrzik et al. 2013). In general, bone is modeled either as a linear elastic or a nonlinear elasto-plastic material with damage, in which the reduction of stiffness is produced by cracks. Bone damage induced during implantation is accounted for by using two approaches: 1) *a priori* stiffness reduction of peripheral bone elements in micro-FE models of a fully bonded implant positioned virtually in intact bone (Steiner et al., 2016, 2017). 2) *a priori* press-fit condition in stress or strain on homogenized FE models assuming fully bonded (Inzana et al., 2016) or frictional contact at the interface (Spears et al., 2001; Berahmani et al., 2017). Direct simulation of the implantation process by implicit FEA leads to excessive damage and severe convergence problems. Explicit methods overcome the aforementioned difficulties by deleting highly distorted elements and facilitating the enforcement of contact conditions (Payan, 2012; Hambli, 2013). In the explicit micro-FE approach, the total implantation procedure is captured using nonlinear bone material, however, two limitations exist. First, the elements get deleted based on a certain value of plastic strain that needs to be adjusted based on the element size and the loading configuration of the bone-

* Corresponding author at: ARTORG Center, University of Bern, Freiburgstrasse 3, 3010 Bern, Switzerland.
E-mail address: marzieh.ovesy@artorg.unibe.ch (M. Ovesy).

https://doi.org/10.1016/j.jbiomech.2020.109844
0021-9290/

implant system. Second, resolution of such models is restricted to small sizes and applying the same procedure on real bone geometries would be computationally too expensive (Ovesy et al., 2019). The existing explicit, homogenized FE approaches account for the BV/TV (bone volume per total volume) variation and enforce contact conditions at the interface while assuming linear elastic bone (Staden et al., 2008; Guan et al., 2011; Affes et al., 2018). Other purely numerical studies assume a Drucker-Prager constitutive law for bone where yield stress is varied in a certain range and a damage evolution was only added to increase stability of the simulation (Dorogoy et al., 2017). According to these previous studies, a damage-based nonlinear material model for the explicit simulation of a bone-implant system has not been developed.

This study aims to develop and validate an explicit finite element method to simulate the insertion of a rigid implant into a deformable bone while accounting for the accumulating damage occurring at the bone-implant interface due to the progressive press-fit. Accordingly, a cyclic press-fit experiment of a conical, titanium implant into a predrilled trabecular bone cylinder is designed and conducted for six samples that delivers the reaction force and the stiffness of the system along the increasing press-fit. Applying similar boundary conditions as the experiment, the explicit finite element model of the bone-implant system is equipped with a homogenized elasto-plastic constitutive model including damage for bone, frictional contact between implant and bone and an element deletion technique to overcome the large strains occurring in the bone during press-fit. The FE model is not only able to reproduce the qualitative structural behavior but also to make quantitative predictions of the growing reaction forces and stiffnesses of the system. A sensitivity analysis is conducted to examine the influence of friction and various element sizes on the computational results.

2. Materials and methods

2.1. Conical press-fit experiment

2.1.1. Bone sample preparation

Six cylindrical trabecular bone samples with 15.5 mm diameter were extracted from bovine proximal tibia along an axis normal to the tibial plateau using the method presented by Voumard et al., 2018 (Fig. 1.A). The samples were fairly homogeneous along the circumferential direction. All samples were then shortened to 25.5 mm and embedded in 8.75 mm layer of polymethyl methacrylate (PMMA) to reproduce the confinement of the cortical shell in dental or orthopedic applications (Fig. 1.B and Fig. 1.D). The pilot hole, with 4 mm of diameter, was drilled stepwise under full numerical control at a rotational speed of 2000 rpm and a feed rate of 1 mm/s.

2.1.2. Cone geometry

The titanium cone was designed in a manner to mimic the compaction exerted by the femoral stem on trabecular bone of the

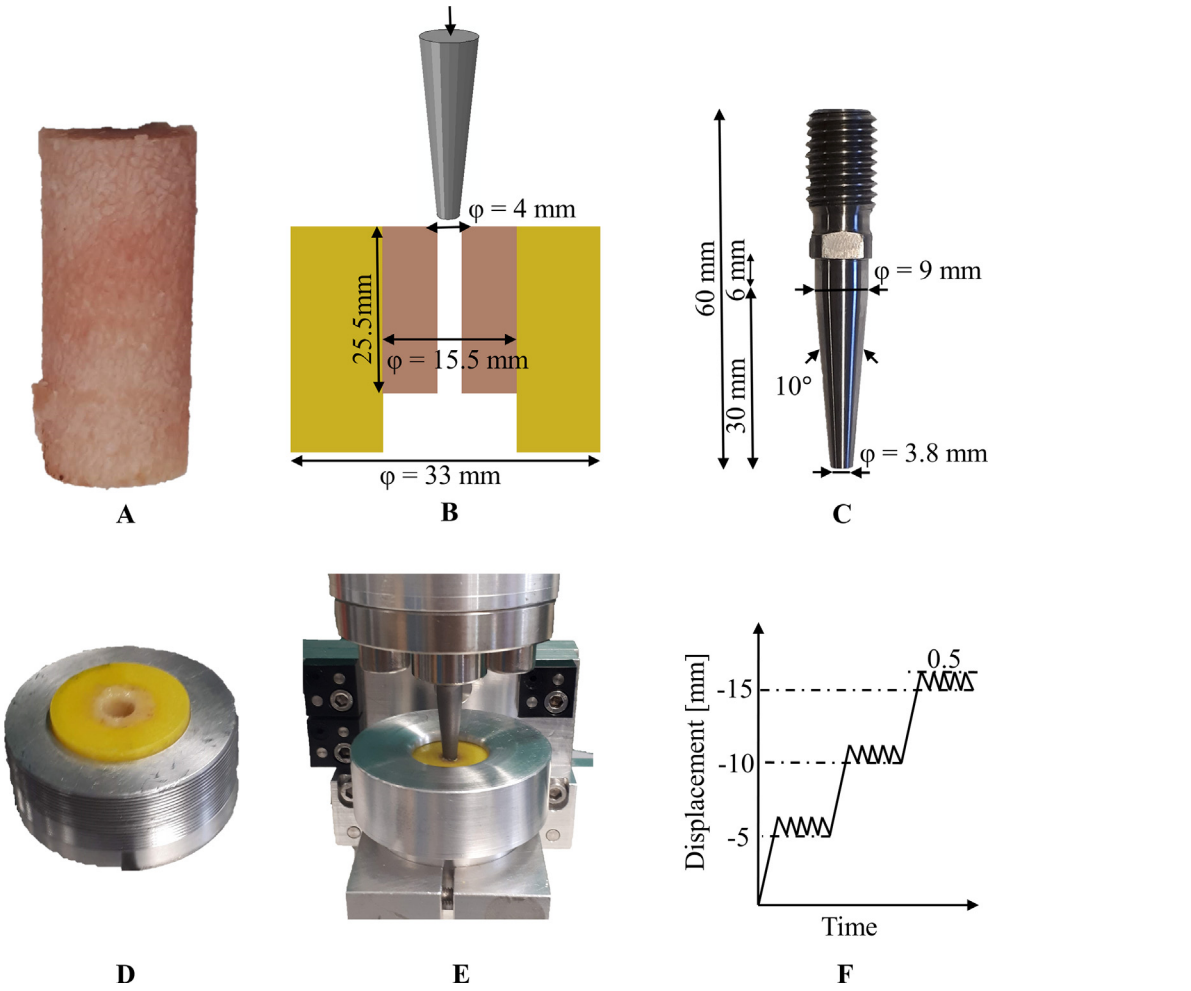

Fig. 1. Cylindrical bovine bone sample (A). The boundary condition of the embedded bone sample (B). The cone geometry (C). Embedded bone sample in PMMA (D). Loading setup (E). Experimental loading protocol (F).

proximal femur. Accordingly, the cone was given an angle of 10○, typical of the proximal part of the femoral implant (Fig. 1.C). After manufacturing, the smooth surface roughness of 0.5 ± 0.01 μm was measured by confocal microscopy (S neox, Sensofar, Spain) at RMS Foundation, Switzerland, based on the ISO 4288 standard.

2.1.3. Loading protocol

The cone was centered on the pilot hole and axially loaded into the trabecular bone samples using a hydraulic actuator (858 Mini bionix, MTS, USA), but was free to move in the transverse plane (Fig. 1.E). The loading protocol consisted of a constant displacement rate of −0.033 mm/s and five loading–unloading cycles with an amplitude of 0.5 mm superimposed at each of the positions −5 mm, −10 mm and −15 mm (Fig. 1.F). The point where the cone initiated contact with the bone sample, was assigned to zero force and displacement. Reaction forces were recorded at the beginning of the first cycles while unloading stiffnesses were computed from the last cycle of the loading–unloading cycle group at each position (Fig. 4).

2.1.4. Imaging of the bone samples

Micro-computed tomography (μCT 100, SCANCO Medical AG, Switzerland) images of the samples were obtained after drilling and again after loading. The original image resolution was 34.4 μm, but the images were coarsened to 69 μm in order to reduce computation time for model generation (Fig. 2.A). The region of interest (ROI) was defined as the bone cylinder excluding the drilled pilot hole and the surrounding PMMA. The images were segmented by using Maximum Entropy Threshold Image Filter provided in SimpleITK library. The threshold value was set to 3200. In order to account for material property heterogeneity, the bone cylinders were divided into five sections in height (every 5 mm) and two sections along the radius forming inner (1.5 mm) and outer regions (Fig. 2.B). BV/TV of all sections was calculated as:

$$BV/TV = \frac{Bone_{volume}}{Bone_{volume} + Marrow_{volume}}$$

where the value of *1* was assigned to the bone voxels and *0* to marrow voxels. In order to compare the reaction force and stiffness at different positions of the cone within the bone sample, a cumulative BV/TV along the height was calculated for each position (Fig. 2.B). The last position deliverd the overall BV/TV of 25.5, 27.3, 28.5, 29.5, 38.0 and 57.0%.

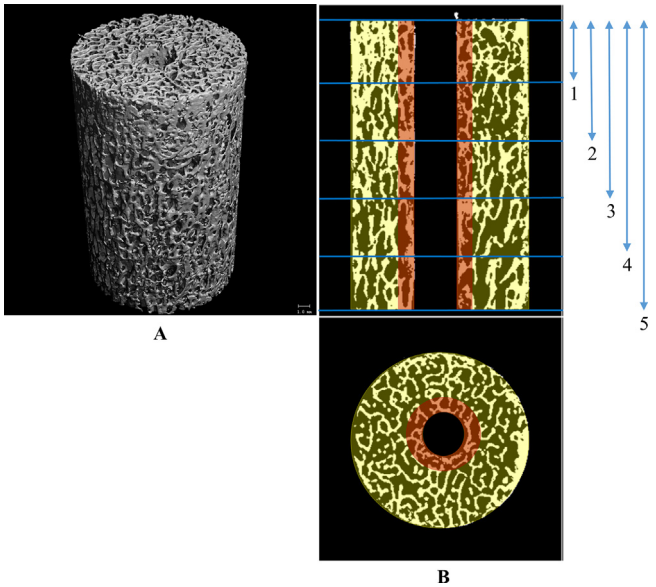

Fig. 2. 3D reconstruction (A) and 2D views with BV/TV divisions (B) of segmented micro-CT scan after drilling with the resolution of 69 μm for the sample with 29.9% of overall BV/TV.

2.2. Finite element model

2.2.1. Model geometry

Bone cylinders of 15.5 mm in diameter and 25.5 mm in height with the drilled hole of 4 mm in diameter were meshed in Abaqus (Abaqus 6.14 Dassault Systems, France) using 11,220 linear hexahedral elements (C3D8) (Fig. 3.B). The element edge size was 2.5 mm in the peripheral section and refined to 0.5 mm in the inner press-fit section. Similar to the corresponding micro-CT images, the bone cylinders were divided into ten element sets to account for the variation of BV/TV (Fig. 3.A).

2.2.2. Material properties

As trabecular orientation was aligned along the pilot hole, the bone material properties were assumed to be transversely isotropic along this axis. An elasto-plastic constitutive model with damage developed for bone by Schwiedrzik et al., 2013 was implemented into a VUMAT subroutine (Appendix A). The material properties were calculated using the BV/TV values assigned to the different sections (Fig. 3.A). The material constants of trabecular bone were scaled from those used by Luisier et al., 2014 to account for the bovine origin of the tissue (Table 1) (;Niebur et al., 2000; Bayraktar et al., 2004; Wang et al., 2006). Since the damage function is defined as a continuous function of the cumulated plastic strains (Wolfram et al., 2011) the bone elements were deleted when reaching 95% of the critical damage value (D_c) (Appendix A). Due to the order of magnitude difference between Young's moduli of titanium and bovine trabecular bone, the cone was considered to be rigid.

2.2.3. Boundary conditions and loading protocol

The boundary conditions and the loading protocol of the FE simulations are presented in Fig. 3.B and Fig. 3.C. The cone was translated along the pilot hole axis throughout the simulation, was free to move in the transverse plane and the rotational degrees of freedom were fixed.

The surface interaction between the cone and the bone sample was modeled as unilateral contact with a friction coefficient of 0.2 (Hefzy and Singh, 1997; MacLeod et al., 2012).

Quasi-static simulations were performed, where variable mass scaling of 0.0001 was used to reduce the analysis time and it was ensured that the kinetic energy remained lower than 5% of the internal energy to restrict the inertial effects. The simulations were run on a Linux based cluster (16 Intel Xeon E5 cores, 256 GB RAM) for an average time of 6 hours per sample.

A force–displacement curve was obtained. Similar to the experiment, a zero-force and position point was defined where the cone showed the initial contact with the bone sample. Three additional force data points were obtained from the positions of the first unloading cycles (red points in Fig. 4). The unloading stiffness of the cone-sample system was again computed from the last loading–unloading cycle at each position.

The number of deleted elements throughout the simulation and bone damage distribution at six stages of insertion were extracted for the sample with a mid-range BV/TV of 29.9%.

2.2.4. Sensitivity analysis

To improve stability and save computing time for the sensitivity analysis, the minimal effect of fixing the cone movement in the *xy* plane was confirmed for the six samples and fixed boundary conditions were then used to conduct the sensitivity analysis on friction and mesh convergence analysis. A mass scaling of 0.001

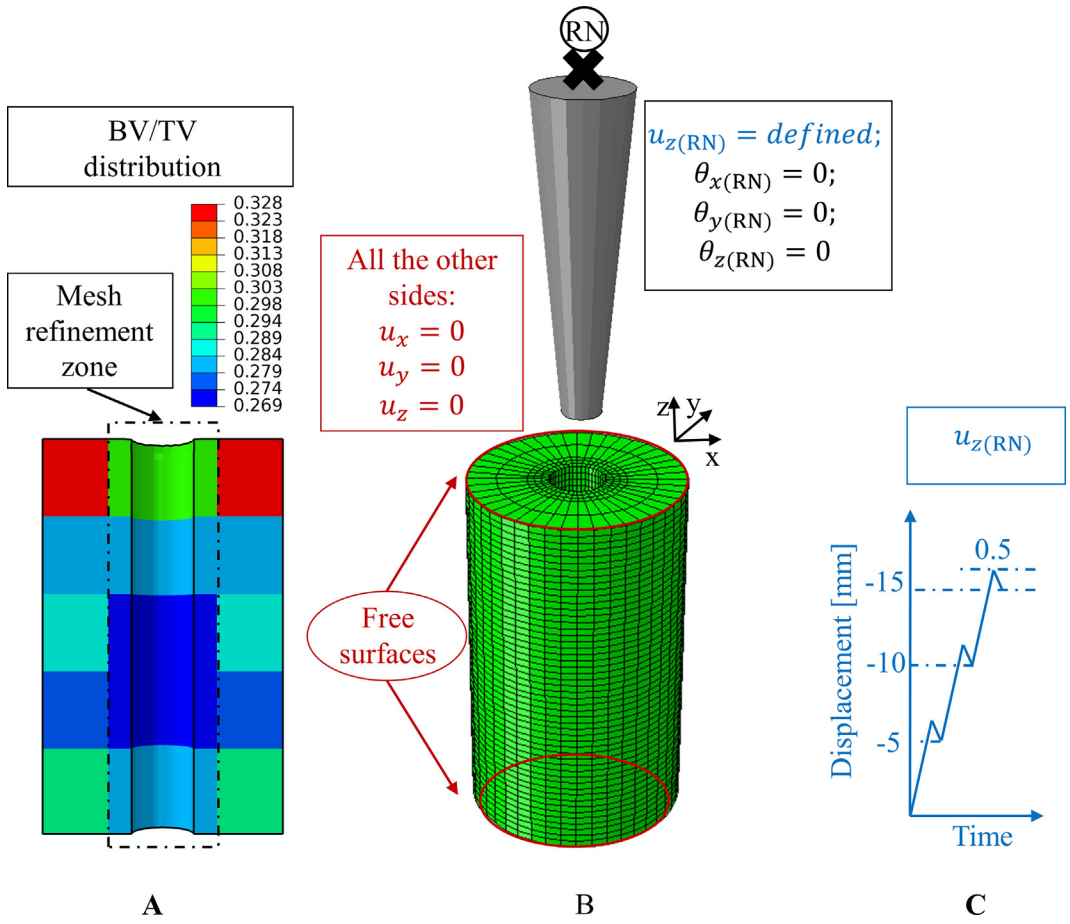

Fig. 3. BV/TV distribution used for the simulation for the sample with the overall BV/TV of 29.9% and the zone considered for mesh refinement (A). Simulation boundary conditions, loading, and mesh (B). Loading protocol for the simulation (C).

Table 1
Elasticity, strength (Luisier et al., 2014) and damage material properties for bovine trabecular bone (Wolfram et al., 2011).

Elasticity					
E_0(GPa)	v_0(-)	k	l		
18	0.249	1.878	1.076		
Strength					
σ_0^+(MPa)	σ_0^-(MPa)	τ_0(MPa)	χ_0(-)	p	q
122.4	167.4	103.4	0.31	1.69	1.05
Damage parameters					
D_c	k_p				
0.85	8.0075				

ensured a low kinetic energy for the fixed boundary conditions and reduced the simulation time to 2 hours per sample.

The friction coefficient was changed from 0.1 to 0.4 (Rancourt et al., 1990; Reggiani et al., 2007) to quantify the influence on reaction force and unloading stiffness (as extracted from Fig. 4). To compensate for the differences among the six samples in this sensitivity analysis, the extracted force and unloading stiffness were normalized by a power function of the cumulated BV/TV of their respective sections (Fig. 3.A) in a manner to achieve the best fit using a friction value of 0.2 for both force and stiffness.

2.2.5. Mesh convergence

Mesh convergence analyses were performed by changing the element edge size at the mesh refinement zone (Fig. 3.A) to 0.3 (fine) and 0.7 mm (coarse), respectively and maintaining the mesh size at the outer boundary the same as before. An additional analysis was conducted to observe the influence of the mesh refinement zone by meshing the whole sample with an element edge size of 0.5 mm.

3. Results

3.1. Finite element validation

3.1.1. Cone insertion, reaction force and unloading stiffness

The experimental force values were passed through a bandpass Butterworth filter using Python signal library (4th order low pass with critical frequency of 2 Hz) to reduce the high-frequency oscillations. As expected from the increase in contact area and as shown in Fig. 4. for the sample with a BV/TV of 29.9%, the experimental force increased throughout the cone insertion. The experimental force–displacement curves of the other samples are provided in the supplementary material. Regardless of some oscillations

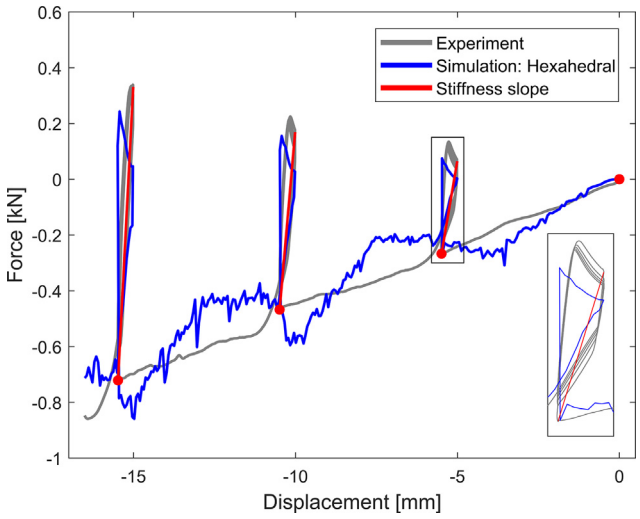

Fig. 4. Force-displacement curve for the sample with BV/TV = 29.9% (gray: experiment, blue: hexahedral simulation, red dots: extracted data points, red lines: extracted stiffness values).

observed in the computed force–displacement curves that we attribute to the sudden reduction of stiffness associated with element deletion, the overall level of the curve is in good qualitative agreement with the experiment (Fig. 4). The loading–unloading loops at the three positions are also rather similar, suggesting the importance of modeling frictional contact between cone and the bone sample.

The oscillations seem not to affect the reaction force extracted at the first unloading cycle because few if any elements are deleted in this mode as seen in Fig. 6.

The strong relationships between experimental and computed reaction force (R^2 = 0.95) and unloading stiffness (R^2 = 0.94) are shown in Fig. 5A and B, respectively.

The damage distribution for the six stages shown in Fig. 6 illustrates the increase in the number of deleted elements with progression of damage.

3.1.2. Sensitivity analysis

Using fixed boundary conditions, a strong correlation was also achieved between experimental force (slope: 1.024, R^2 = 0.96) and stiffness (slope: 0.883, R^2 = 0.94). Fixed boundary condition was therefore used for the sensitivity analyses (see supplementary material).

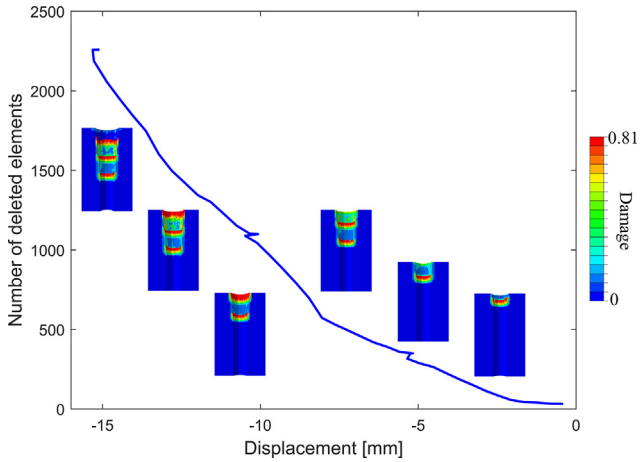

Fig. 6. Damage distribution for six stages and the number of deleted elements for the sample with 29.9% of BV/TV.

The best fit to compensate for the difference among the six samples simulated with the friction coefficient of 0.2 is achieved by normalizing the force and stiffness data by BV/TV with an exponent of 1.8.

The increase in friction coefficient increases the reaction force and stiffness (Fig. 7.A). A power relationship is observed for both normalized force and unloading stiffness with respect to displacement and the power increases with increasing friction coefficient, illustrating the strong effect of friction in this press-fit model (Fig. 7.B and C).

3.1.3. Mesh convergence

The force-dipslacement curves of the mesh convergence analysis for the sample with a BV/TV of 29.9% are shown in Fig. 8 that all demonstrate a very similar behavior. The normalized force at the maximum displacement of 15.5 mm using the calculated fit changed from 13.8% to 9.9% when changing the mesh from coarse to regular and regular to fine, respectively. Using the same extraction procedure for the normalized stiffness values, changing from coarse to regular mesh had 11% of effect on the results at the dis-

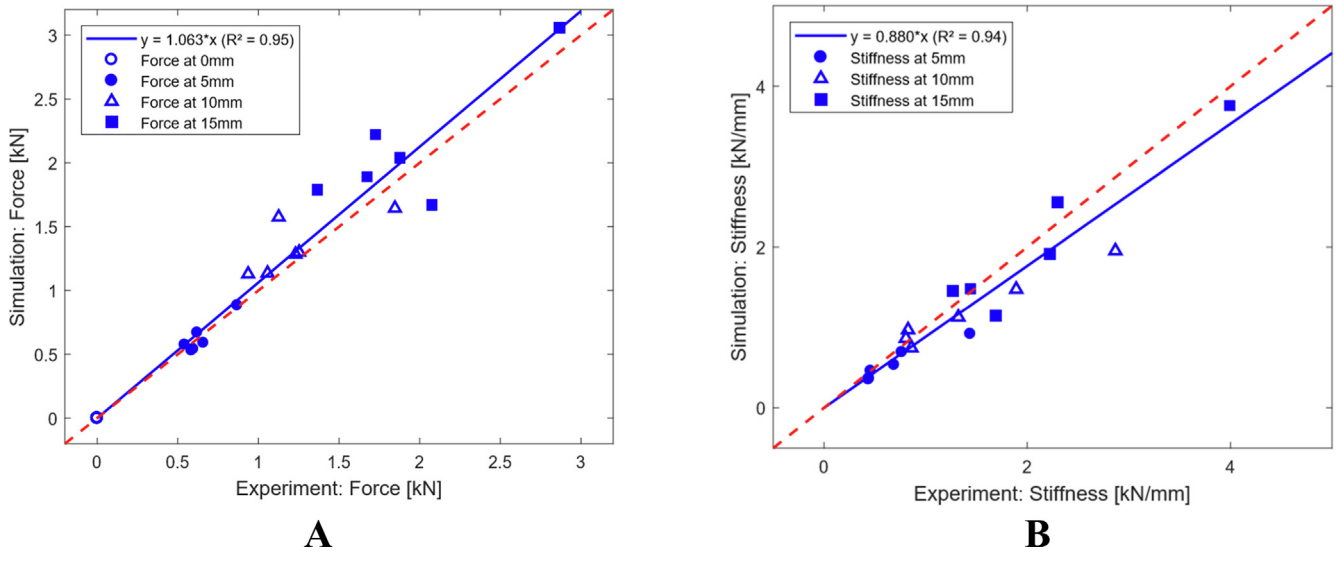

Fig. 5. Correlation between experiment and simulation for the force–displacement data points (A) and unloading stiffness (B).

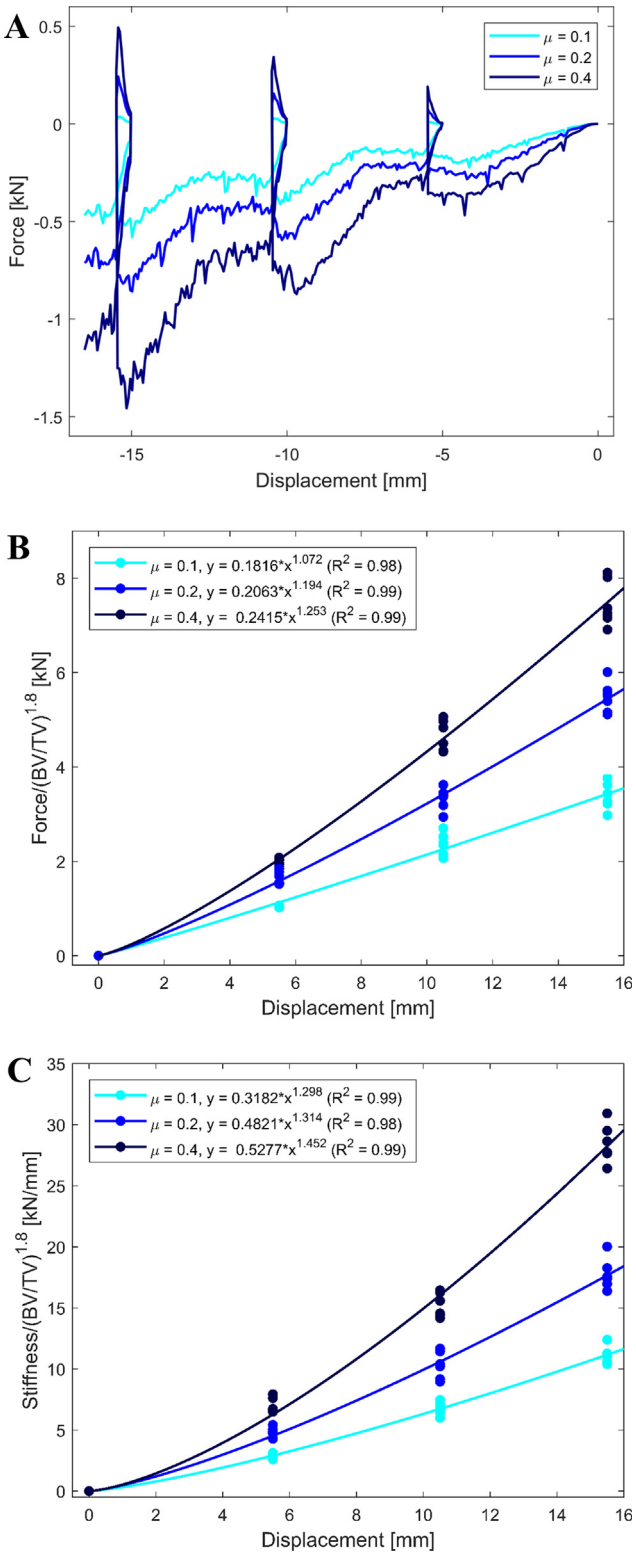

Fig. 7. Effect of friction on the overall force–displacement curve for the sample with 29.9% of BV/TV (A), normalized force–displacement (B) and normalized unloading stiffness-displacement curves (C) (light blue: 0.1, blue: 0.2 and dark blue: 0.4).

placement of 15.5 mm, whereas it altered the values by 6% when using the fine mesh instead of the regular mesh. Although perceptible, mesh convergence remains above 5% for the regular mesh, but the fine mesh requires excessive computational resources for the full study (see supplementary material).

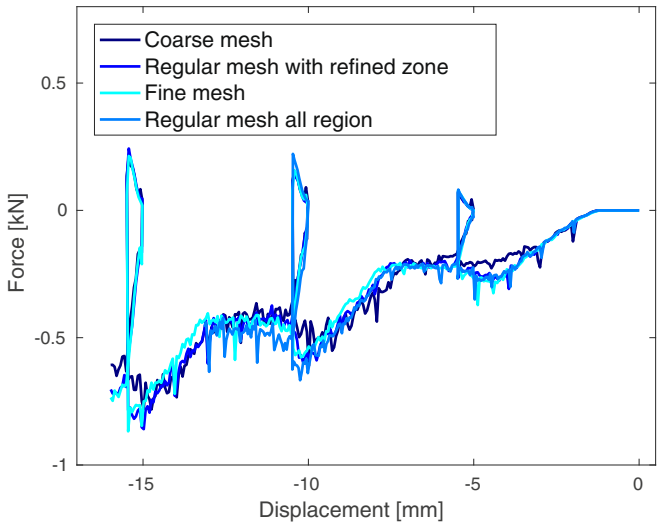

Fig. 8. Force-displacement curves for the sample with BV/TV = 29.9% for different meshing strategies of coarse, fine, regular with and without refined zone.

4. Discussion

In this study, an explicit formulation of the implicit bone damage model proposed by Schwiedrzik et al., 2013 was implemented in the Abaqus software and applied to a conical press-fit problem. The model aimed to provide a better insight into the insertion process and the resulting primary stability of bone-implant systems in terms of stiffness. An experiment was designed where a rigid cone was progressively inserted in cylindrical hollow trabecular bone samples with a servo-hydraulic testing system and structural stiffness was quantified at various levels of press-fit. Both monotonic cone insertion and stepwise interrogation of stiffness were then simulated with an explicit finite element scheme for six bone samples. Sensitivity analysis for the friction coefficient was performed and a brief convergence analysis for the mesh was completed.

The insertion force increased with translation of the cone in both experiment and simulation. This trend was still observed when the force was normalized with BV/TV of the press-fit section and is attributed to the growing contact area between cone and sample (Rong and Huang, 2005). This is in accordance with the linear increase in force observed in other press-fit experiments (Bishop et al., 2014; Damm et al., 2017). The cyclic loops visualized in both simulation and experiment also resemble the loops reported in the literature due to coupling of axial translation, normal and frictional forces (Kaze et al., 2015).

The modeling approach proposed in this work has several benefits for the simulation of bone-implant systems.

First, it can reproduce the large deformations associated with implant insertion by deleting the highly distorted elements and then extract the resulting stiffness reflecting primary stability of the implant. Unlike previous methods, there is no need to account for the actual amount of damage based on the post-implanted image analysis as damage is introduced through the flow of plastic strains on the defined yield surface. In addition, although some models do not account for the variation of BV/TV in trabecular bone, this model is based on averaging the bone properties in a certain vicinity. In homogenized models, the number of elements is much lower than in micro-FE models, enabling the simulation of larger geometries (for instance a femoral shaft) in an acceptable time. In this study, ten sections with distinct material properties were sufficient to capture the heterogeneity of the samples.

Second, applying frictional contact at the bone-implant interface gives insight into the effect of implant design and surface

treatment on micromotions and potential loosening of implant that is not achievable using fully bonded models. The increasing friction coefficient resulted in augmentation of both force and stiffness that is attributed to the larger shear forces at the interface (Kelly et al., 2013). In addition, the explicit solver can overcome the convergence problems occurring with implicit solvers when elements undergo large distortions.

Nevertheless, this study also has several limitations. First, the stiffness reduction due to element deletion in the FE analysis produces oscillations in the force–displacement curves (Werner et al., 2019). However, the oscillations did not seem to play a significant role in the extraction of the force and stiffness values when using different types of elements. Developing a nonlocal damage model in the explicit scheme by either averaging the damage parameter in a certain region (Hosseini et al., 2015) or adding corrective forces to the surrounding elements (Harrison et al., 2013) could reduce these oscillations. The oscillations may be reduced by increasing the number of elements in the model and therefore reduction of the stiffness variation due to element deletion. However, this would require excessive computational resources for an explicit approach. Second, the use of a simple cone geometry for the implant and the use of transversely isotropic bovine trabecular bone without cortical shell. This was done to focus on the press-fit principle rather than a specific type of implant and to ease the comparison among bone samples by reducing geometrical and BV/TV variations. In addition, the conical shape allowed to increase the contact area of the implant with the bone along the insertion process similar to numerous clinical applications. Third, the use of single damage variable in the constitutive model that reduces bone stiffness in the same manner in both shear and hydrostatic compression. The introduction of multiple damage variables such as the model proposed by Levrero-Florencio and Pankaj, 2018 may allow a better description of the softening behavior of the bone-implant interface for different ratios of compaction and shear stresses. Overcoming this limitation requires a more sophisticated experiment that was out of the focus of this study.

5. Conclusion

The developed explicit homogenized finite element approach allows simulating insertion of a rigid implant in frictional contact with a continuous bone mesh that undergoes large deformations and avoids excessive element distortions by triggering element deletion. The approach accounts for bone damage produced by implant insertion and provides a fair estimation of both reaction force and structural stiffness. The time associated with image processing, meshing and computation is strongly reduced when compared to previous strategies. Following this encouraging proof of concept with a conical implant geometry, the developed explicit finite element methodology can be applied to estimate the primary stability of bone-implant systems and simulate micromotions at the interface in dental and orthopedic applications.

Declaration of Competing Interest

The authors declare that they have no known competing financial interests or personal relationships that could have appeared to influence the work reported in this paper.

Acknowledgment

We would like to gratefully acknowledge Benjamin Voumard for his support during the experiments, Michael Indermaur for realizing the image registration and the RMS Foundation, Bettlach, Switzerland for grant no. E16_0001/HOM-FEM.

Appendix A. Bone constitutive model

An existing implicit material modeling for bone proposed by Schwiedrzik et al., 2013 based on the second Piola-Kirchhoff stress and Green Lagrange strain was chosen and adapted to be implemented in the explicit solver scheme. In this model, bone is assumed to exhibit an elasto-plastic behaviour with damage and a quadric yield surface. The material constants of bone depend on BV/TV and a fabric tensor **M** characterizing material anisotropy (Matsuura et al., 2008; Zysset and Curnier, 1995). In Abaqus explicit scheme (VUMAT), the Cauchy stress (**T**) needs to be updated in each increment:

$$\mathbf{T} = (1 - D(\kappa))\mathbb{T}(\mathbf{E} - \mathbf{E}^p) \tag{1}$$

where **E** and $\mathbf{E}^p$ are the total and plastic strain tensors, respectively and $\mathbb{T}$ represents the fourth-order material stiffness tensor. The stress is reduced using damage function ($D(\kappa)$) that is defined based on cumulated plastic strain (κ) throughout time (t):

$$D(\kappa) = D_c.(1 - e^{-k_p\kappa}) \tag{2}$$

$$\kappa = \int_0^t \|\dot{\mathbf{E}}^p\| d\tau \tag{3}$$

where (D_c) and (k_p) are constants and ($\dot{\mathbf{E}}^p$) is the rate of the plastic strain tensor.

In the explicit scheme by applying the central difference theory on the position vectors at the end ($\boldsymbol{x}(t + \Delta t)$) and beginning ($\boldsymbol{x}(t)$) of the time increment, the velocity vector at the middle point of the time increment ($\boldsymbol{v}(t + \frac{\Delta t}{2})$) is calculated (Nemat-Nasser, 2004):

$$\boldsymbol{x}(t + \Delta t) = \boldsymbol{x}(t) + \boldsymbol{v}\left(t + \frac{\Delta t}{2}\right).\Delta t \tag{4}$$

Under the assumption of small-time increments and applying the central difference theory to the deformation gradient tensor (**F**):

$$\mathbf{F}(t + \frac{\Delta t}{2}) = \frac{1}{2}(\mathbf{F}(t + \Delta t) + \mathbf{F}(\mathrm{t})) \tag{5}$$

$$\mathbf{F}(t + \Delta t) = \mathbf{F}(\Delta t)\mathbf{F}(\mathrm{t}) \tag{6}$$

$$\dot{\mathbf{F}}\left(\boldsymbol{t} + \frac{\Delta \boldsymbol{t}}{2}\right) = \frac{\mathbf{F}(t + \Delta t) - \mathbf{F}(\mathrm{t})}{\Delta t} \tag{7}$$

the velocity gradient tensor (**L**) is driven by the following equations:

$$\mathbf{L}\left(t + \frac{\Delta t}{2}\right) = \dot{\mathbf{F}}\left(t + \frac{\Delta t}{2}\right).\mathbf{F}^{-1}\left(t + \frac{\Delta t}{2}\right) = \frac{2}{\Delta t}(\mathbf{F}(\Delta t) - \mathbf{I})(\mathbf{F}(\Delta t) + \mathbf{I})^{-1} \tag{8}$$

Using tensor (**L**), the strain rate tensor (**D**) and the spin tensors (**W**) are defined as:

$$\mathbf{D} = \frac{1}{2}(\mathbf{L} + \mathbf{L}^T) \tag{9}$$

$$\mathbf{W} = \frac{1}{2}(\mathbf{L} - \mathbf{L}^T) \tag{10}$$

In the VUMAT the strain increment, the deformation gradient tensor at the beginning and the end of the time increment are given by the subroutine, however, the strain tensor needs to be defined as follows:

$$\mathbf{E}(t + \Delta t) = \mathbf{E}(t) + \mathbf{D}\left(t + \frac{\Delta t}{2}\right).\Delta t \tag{11}$$

In addition, the total strain, the plastic strain, and the stress tensors need to be rotated from the element coordinate system to the material coordinate system at the beginning of the subroutine and back rotated at the end of the increment.

Hughes and Winget, 1980 proposed the proper orthogonal incremental rotation tensor ($\mathbf{R}$) as:

$$\mathbf{R}(t+\Delta t)=\left(\mathbf{I}-\frac{\mathbf{W}}{2}\Delta t\right)^{-1}\left(\mathbf{I}+\frac{\mathbf{W}}{2}\Delta t\right) \tag{12}$$

where it is proven that $\mathbf{R}\mathbf{R}^{T}=\mathbf{I}$.

Appendix B. Supplementary data

Supplementary data to this article can be found online at https://doi.org/10.1016/j.jbiomech.2020.109844.

References

Affes, F., Ketata, H., Kharrat, M., Dammak, M., 2018. How a pilot hole size affects osteosynthesis at the screw–bone interface under immediate loading. Med. Eng. Phys. 60, 14–22. https://doi.org/10.1016/j.medengphy.2018.07.002.

Bah, M.T., Shi, J., Heller, M.O., Suchier, Y., Lefebvre, F., Young, P., King, L., Dunlop, D. G., Boettcher, M., Draper, E., Browne, M., 2015. Inter-subject variability effects on the primary stability of a short cementless femoral stem. J. Biomech. 48, 1032–1042. https://doi.org/10.1016/j.jbiomech.2015.01.037.

Bayraktar, H.H., Morgan, E.F., Niebur, G.L., Morris, G.E., Wong, E.K., Keaveny, T.M., 2004. Comparison of the elastic and yield properties of human femoral trabecular and cortical bone tissue. J. Biomech. 37, 27–35. https://doi.org/10.1016/S0021-9290(03)00257-4.

Berahmani, S., Janssen, D., Verdonschot, N., 2017. Experimental and computational analysis of micromotions of an uncemented femoral knee implant using elastic and plastic bone material models. J. Biomech. 61, 137–143. https://doi.org/10.1016/j.jbiomech.2017.07.023.

Bishop, N.E., Höhn, J.C., Rothstock, S., Damm, N.B., Morlock, M.M., 2014. The influence of bone damage on press-fit mechanics. J. Biomech. 47, 1472–1478. https://doi.org/10.1016/j.jbiomech.2014.01.029.

Charlebois, M., Jirásek, M., Zysset, P.K., 2010. A nonlocal constitutive model for trabecular bone softening in compression. Biomech. Model. Mechanobiol. 9, 597–611. https://doi.org/10.1007/s10237-010-0200-3.

Damm, N.B., Morlock, M.M., Bishop, N.E., 2017. Influence of trabecular bone quality and implantation direction on press-fit mechanics. J. Orthop. Res. 35, 224–233. https://doi.org/10.1002/jor.23257.

Dorogoy, A., Rittel, D., Shemtov-Yona, K., Korabi, R., 2017. Modelling dental implant insertion. J. Mech. Behav. Biomed. Mater. 68, 42–50. https://doi.org/10.1016/j.jmbbm.2017.01.021.

Guan, H., Van Staden, R.C., Johnson, N.W., Loo, Y.C., 2011. Dynamic modelling and simulation of dental implant insertion process-A finite element study. Anal. Des. Finite Elem. https://doi.org/10.1016/j.finel.2011.03.005.

Hambli, R., 2013. A quasi-brittle continuum damage finite element model of the human proximal femur based on element deletion. Med. Biol. Eng. Comput. 51, 219–231. https://doi.org/10.1007/s11517-012-0986-5.

Harrison, Noel M., McDonnell, Pat, Mullins, Liam, Wilson, Niall, O'Mahoney, Denis, McHugh, Peter E., 2013. Failure modelling of trabecular bone using a non-linear combined damage and fracture voxel finite element approach. Biomech Model Mechanobiol 12 (2), 225–241. https://doi.org/10.1007/s10237-012-0394-7.

Hefzy, M.S., Singh, S.P., 1997. Comparison between two techniques for modelling interface conditions in a porous coated hip endoprosthesis. Med. Eng. Phys. 19, 50–62.

Hosseini, H.S., Horák, M., Zysset, P.K., Jirásek, M., 2015. An over-nonlocal implicit gradient-enhanced damage-plastic model for trabecular bone under large compressive strains. Int. j. numer. method. biomed. eng, 31.

Hosseini, H.S., Pahr, D.H., Zysset, P.K., 2012. Modeling and experimental validation of trabecular bone damage, softening and densification under large compressive strains. J. Mech. Behav. Biomed. Mater. 15, 93–102.

Hughes, T.J.R., Winget, J., 1980. Finite rotation effects in numerical integration of rate constitutive equations arising in large-deformation analysis. Int. J. Numer. Methods Eng. 15, 1862–1867.

Inzana, J.A., Varga, P., Windolf, M., 2016. Implicit modeling of screw threads for efficient finite element analysis of complex bone-implant systems. J. Biomech. 49, 1836–1844. https://doi.org/10.1016/j.jbiomech.2016.04.021.

Jasty, M., Bragdon, C., Burke, D., O'Connor, D., Lowenstein, J., Harris, W.H., 1997. In vivo skeletal responses to porous-surfaced implants subjected to small induced motions. JBJS 79, 707–714.

Kaze, A.D., Maas, S., Waldmann, D., Zilian, A., Dueck, K., Pape, D., 2015. Biomechanical properties of five different currently used implants for open-wedge high tibial osteotomy. J. Exp. Orthop. 2, 14.

Kelly, N., Cawley, D.T., Shannon, F.J., Mcgarry, J.P., 2013. Medical Engineering & Physics An investigation of the inelastic behavior of trabecular bone during the press-fit implantation of a tibial component in total knee arthroplasty. Med. Eng. Phys. 35, 1599–1606. https://doi.org/10.1016/j.medengphy.2013.05.007.

Levrero-Florencio, F., Pankaj, P., 2018. Using Non-linear Homogenization to Improve the Performance of Macroscopic Damage Models of Trabecular Bone. Front, Physiol, p. 9.

Luisier, B., Dall'Ara, E., Pahr, D.H., 2014. Orthotropic HR-pQCT-based FE models improve strength predictions for stance but not for side-way fall loading compared to isotropic QCT-based FE models of human femurs. J. Mech. Behav. Biomed. Mater. 32, 287–299. https://doi.org/10.1016/j.jmbbm.2014.01.006.

MacLeod, A.R., Pankaj, P., Simpson, A.H.R.W., 2012. Does screw-bone interface modelling matter in finite element analyses? J. Biomech. 45, 1712–1716. https://doi.org/10.1016/j.jbiomech.2012.04.008.

Matsuura, M., Eckstein, F., Lochmüller, E.-M., Zysset, P.K., 2008. The role of fabric in the quasi-static compressive mechanical properties of human trabecular bone from various anatomical locations. Biomech. Model. Mechanobiol. 7, 27–42.

Mjöberg, B., 1997. The theory of early loosening of hip prostheses. Orthopedics 20, 1169–1175. https://doi.org/10.3928/0147-7447-19971201-12.

Nemat-Nasser, S., 2004. Plasticity: a treatise on finite deformation of heterogeneous inelastic materials. Cambridge University Press.

Niebur, G.L., Feldstein, M.J., Yuen, J.C., Chen, T.J., Keaveny, T.M., 2000. High-resolution finite element models with tissue strength asymmetry accurately predict failure of trabecular bone. J. Biomech 1575–1583. https://doi.org/10.1016/S0021-9290(00)00149-4.

Ovesy, M., Indermaur, M., Zysset, P.K., 2019. Prediction of insertion torque and stiffness of a dental implant in bovine trabecular bone using explicit micro-finite element analysis. J. Mech. Behav. Biomed. Mater. 98, 301–310. https://doi.org/10.1016/j.jmbbm.2019.06.024.

Payan, Y., 2012. Soft tissue biomechanical modelling for computer assisted surgery. Springer.

Pilliar, R.M., Lee, J.M., Maniatopoulos, C., 1986. Observations on the effect of movement on bone ingrowth into porous-surfaced implants. Clin. Orthop. Relat. Res., 108–113.

Rancourt, D., Shirazi-Adl, A., Drouin, G., Paiement, G., 1990. Friction properties of the interface between porous-surfaced metals and tibial cancellous bone. J. Biomed. Mater. Res. 24, 1503–1519.

Reggiani, B., Cristofolini, L., Varini, E., Viceconti, M., 2007. Predicting the subject-specific primary stability of cementless implants during pre-operative planning: Preliminary validation of subject-specific finite-element models. J. Biomech. 40, 2552–2558. https://doi.org/10.1016/j.jbiomech.2006.10.042.

Rong, Y.K., Huang, S., 2005. Advanced computer-aided fixture design. Elsevier.

Schwiedrzik, J.J., Wolfram, U., Zysset, P.K., 2013. A generalized anisotropic quadric yield criterion and its application to bone tissue at multiple length scales. Biomech. Model. Mechanobiol. 12, 1155–1168.

Spears, I.R., Pfleiderer, M., Schneider, E., Hille, E., Morlock, M.M., 2001. The effect of interfacial parameters on cup-bone relative micromotions A finite element investigation. J. Biomech. https://doi.org/10.1016/S0021-9290(00)00112-3.

van Staden, Rudi C., Guan, Hong, Johnson, Newell W., Loo, Yew-Chaye, Meredith, Neil, 2008. Step-wise analysis of the dental implant insertion process using the finite element technique. Clin Oral Implants Res 19 (3), 303–313. https://doi.org/10.1111/clr.2008.19.issue-310.1111/j.1600-0501.2007.01427.x.

Steiner, J.A., Christen, P., Affentranger, R., Ferguson, S.J., van Lenthe, G.H., 2017. A novel in silico method to quantify primary stability of screws in trabecular bone. J. Orthop. Res. 1–11. https://doi.org/10.1002/jor.23551.

Steiner, J.A., Ferguson, S.J., van Lenthe, G.H., 2016. Screw insertion in trabecular bone causes peri-implant bone damage. Med. Eng. Phys. 38, 417–422. https://doi.org/10.1016/j.medengphy.2016.01.006.

van der Ploeg, B., Tarala, M., Homminga, J., Janssen, D., Buma, P., Verdonschot, N., 2012. Toward a more realistic prediction of peri-prosthetic micromotions. J. Orthop. Res. 30, 1147–1154.

van Rietbergen, B., Ito, K., 2015. A survey of micro-finite element analysis for clinical assessment of bone strength: The first decade. J. Biomech. 48, 832–841. https://doi.org/10.1016/j.jbiomech.2014.12.024.

Voumard, B., Maquer, G., Heuberger, P., Zysset, P.K., Wolfram, U., 2018. Peroperative Estimation of Bone Quality and Primary Dental Implant Stability. J. Mech. Behav. Biomed. Mater. 92, 24–32. https://doi.org/10.1016/j.jmbbm.2018.12.035.

Wang, X.J., Chen, X.B., Hodgson, P.D., Wen, C.E., 2006. Elastic modulus and hardness of cortical and trabecular bovine bone measured by nanoindentation. Trans. Nonferrous Met. Soc. China (English Ed. 16. https://doi.org/10.1016/S1003-6326(06)60293-8.

Werner, Benjamin, Ovesy, Marzieh, Zysset, Philippe K., 2019. An explicit micro-FE approach to investigate the post-yield behaviour of trabecular bone under large deformations. Int J Numer Meth Biomed Engng 35 (5), e3188. https://doi.org/10.1002/cnm.v35.510.1002/cnm.3188.

Wolfram, U., Wilke, H.J., Zysset, P.K., 2011. Damage accumulation in vertebral trabecular bone depends on loading mode and direction. J. Biomech. 44, 1164–1169. https://doi.org/10.1016/j.jbiomech.2011.01.018.

Wyatt, M., Hooper, G., Frampton, C., Rothwell, A., 2014. Survival outcomes of cemented compared to uncemented stems in primary total hip replacement. World J. Orthop. 5, 591.

Zysset, P., Curnier, A., 1995. An alternative model for anisotropic elasticity based on fabric tensors. Mechanics of Materials 21 (4), 243–250.